

Simulation of alnico coercivity

Liqin Ke,^{1,*} Ralph Skomski,² Todd D. Hoffmann,³ Lin Zhou,¹ Wei Tang,¹
Duane D. Johnson,^{1,4} Matthew J. Kramer,¹ Iver E. Anderson,¹ and C.-Z. Wang¹

¹Ames Laboratory, U.S. Department of Energy, Ames, Iowa 50011, USA

²Department of Physics and Astronomy, University of Nebraska, Lincoln, Nebraska 68588, USA
³1137 W Emerald Ave, Mesa, Arizona 85210, USA

⁴Department of Materials Science & Engineering, Iowa State University, Ames, Iowa 50011, USA

(Dated: October 27, 2021)

Micromagnetic simulations of alnico show substantial deviations from Stoner-Wohlfarth behavior due to the unique size and spatial distribution of the rod-like Fe-Co phase formed during spinodal decomposition in an external magnetic field. The maximum coercivity is limited by single-rod effects, especially deviations from ellipsoidal shape, and by interactions between the rods. Both the exchange interaction between connected rods and magnetostatic interaction between rods are considered, and the results of our calculations show good agreement with recent experiments. Unlike systems dominated by magnetocrystalline anisotropy, coercivity in alnico is highly dependent on size, shape, and geometric distribution of the Fe-Co phase, all factors that can be tuned with appropriate chemistry and thermal-magnetic annealing.

The anisotropy of most permanent magnets is of magnetocrystalline origin, meaning that hysteresis and coercivity rely on the atomic-scale interplay between spin-orbit coupling and crystal-field interaction [1–3]. Alnico magnets—a family of nanostructured alloys consisting primarily of Fe, Al, Ni, and Co—are an exception, because their magnetic anisotropy and hysteresis originate almost entirely from magnetostatic dipole-dipole interactions [4–7]. These materials have attracted renewed attention in the context of magnetic materials that are free of rare-earth elements and do not contain other expensive elements, such as Pt [7–14]. The magnetic anisotropy of alnicos reflects their peculiar nanostructure, where high-magnetization rods with an approximate composition of FeCo (α_1 -phase) are embedded in an essentially nonmagnetic Al-Ni-rich matrix (α_2 -phase) [4–7, 14–18].

There are several grades of alnico magnets, characterized by different chemical compositions and microstructures. We focus on a high quality grade, namely, alnico 8. Figure 1 shows a high-angle-annular-dark-field (HAADF) scanning transmission electron microscopy (STEM) image of an alnico 8 sample along the longitudinal direction. The α_1 rods in the sample of Fig. 1 have diameters of ~ 25 – 45 nm and lengths of ~ 100 – 600 nm and are uniformly distributed in the α_2 matrix. Some of the α_1 rods have pointy ends and/or touch each other. The detailed microstructures strongly depend on alloy composition and heat treatment conditions. Details of alnico alloy fabrication and microstructure characterization are reported elsewhere [7, 19].

Alnico magnets have high Curie temperatures and magnetizations, but their modest coercivity limits the performance of this otherwise very good permanent-magnet material. Surprisingly, the understanding of alnico coercivity in terms of the dipolar anisotropy has remained very poor quantitatively and even qualitatively.

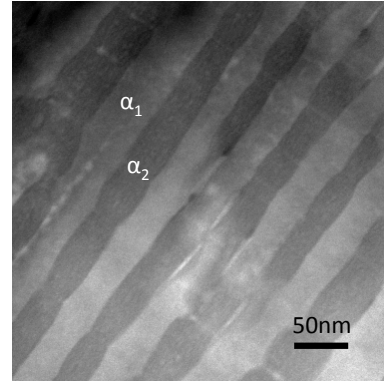


FIG. 1. HAADF STEM image showing a side view of α_1 rods distributed in the α_2 matrix in an alnico 8 alloy.

The main reason is the multiscale character of the calculations, which involves local features having sizes of less than 5 nm, but ranging to interactions on scales comparable to or exceeding the wire length of about $1 \mu\text{m}$. Only recently, computer power has become sufficient to treat interactions between the rods. In this letter, we present micromagnetic simulations [20] to quantitatively explain the coercivity of alnico magnets. In particular, we show and analyze how the coercivity depends on structural features, namely, the shape of the rod ends, the spatial arrangements of Fe-Co rods in the magnet, and the crossing and/or branching of rods.

The conventional explanation of alnico anisotropy is shape anisotropy similar to that of small, elongated Stoner-Wohlfarth particles [21, 22]. In this approximation, an aligned magnetic rod or “elongated fine particle” is subject to a mean-field-like interaction with neighboring rods, and the corresponding coercivity is given by the semi-empirical formula [21]

$$H_c = (1 - p)(N_\perp - N_\parallel)M_s. \quad (1)$$

Here, $N_\perp \approx 1/2$ and $N_\parallel \approx 0$ are the demagnetization fac-

* Corresponding author: liqinke@ameslab.gov

tors perpendicular and parallel to each rod's long axis, M_s is the magnetization of the rods, and p is their packing fraction in the nonmagnetic matrix. However, the coherent-rotation or Stoner-Wohlfarth model has several limitations.

First, it is limited to rods of very small diameters, less than $2R_{\text{coh}} \approx 20$ nm [23–25], whereas typical alnico rods have diameters of the order of $2R = 40$ – 50 nm (Fig. 1). In such relatively thick rods, the magnetization reversal starts by magnetization curling, for which the nucleation field is described by [6, 23–27]

$$H_c = \frac{2K_1}{\mu_0 M_s} - N_{\parallel} M_s + \frac{c(N_{\parallel})A}{\mu_0 M_s R^2}. \quad (2)$$

Here, K_1 is the magnetocrystalline anisotropy constant, A is the exchange stiffness [28], and the values of c are 8.666 for spheres ($N_{\parallel} = 1/3$) and 6.678 for needles ($N_{\parallel} = 0$). In alnicos, the K_1 term is small compared to the magnetostatic terms, contributing only about 10% to H_c [29], and usually neglected [13, 21]. In Eq. (1), the difference $N_{\perp} - N_{\parallel} = 1 - 3N_{\parallel}$ is positive for $N_{\parallel} < 1/3$ (shape anisotropy), but the corresponding curling term $-N_{\parallel} M_s$ in Eq. (2) is always negative. The last term in Eq. (2) partially compensates the coercivity loss due to curling but depends on the radius R . Since alnico rods are thick enough that reversal starts via curling, it is simplistic to interpret alnico anisotropy as shape anisotropy [25, 30]. In reality, $-N_{\parallel} M_s$ is negative but small enough that the exchange term in Eq. (2) ensures a positive coercivity unless the rod diameter $2R$ is very large. In practice, the diameter—determined by the spinodal decomposition process—is sufficiently small to contribute some coercivity but not small enough to reach the Stoner-Wohlfarth limit of Eq. (1).

Second, Eqs. (1–2) are only valid for ellipsoids. For real structures other than ellipsoidal shapes, N_{\perp} and N_{\parallel} are no longer well-defined, and the non-ellipsoidal shapes have smaller coercivity than the ellipsoidal shape [24, 25, 31]. This complication, commonly referred to as Brown's paradox, can be resolved only by explicit consideration of the magnet's real structure (bulk microstructure).

Third, interactions between rods are simplistically treated in Eq. (1) and formally ignored in Eq. (2). To be precise, Eq. (1) replaces the complicated magnetostatic interaction by a p -dependent mean field. The coercivity is the largest for distantly spaced rods ($p \approx 0$) but vanishes completely in the limit of continuous soft-magnetic thin films ($p = 1$). The energy product, which succinctly expresses the performance of a permanent magnet, reaches its maximum at $p = 2/3$ in this approximation [13, 32], agreeing fairly well with experiment. The same magnetostatic interaction effect could be included in Eq. (2) by introducing effective demagnetizing factors [33], but this does not alleviate the basic shortcomings of the approximation. In fact, the coercivity strongly depends on the spatial arrangement of the magnetic rods, as we will see below.

Fourth, it is known experimentally that the rods or

“wires” of the magnetic phase undergo crossing and branching [6, 7, 14]. These features are likely to strongly affect coercivity, and their treatment requires demanding numerical calculations. In the theoretical literature, this effect has not been addressed so far.

To simulate the coercivity, we model the alnicos as aligned or “anisotropic” magnets consisting of parallel magnetic rods, thereby establishing a unique \parallel (parallel) axis. This structural model reproduces the key feature of alnico microstructure, namely, magnetic rods in an essentially nonmagnetic matrix (Fig. 1). Some alnicos have rod orientations that differ from the global magnetization axis, i.e., the rods are misaligned [6, 7, 14]. This case is physically very different [34] from the presently aligned rods and goes beyond the scope of the present paper.

Our calculations use the recently developed MUMAX3 micromagnetics code [35]. We employed either clusters of particles or periodic boundary conditions (PBCs) to investigate the interactions between rods. In our calculations, we used a 1 nm grid and 1 Oe field steps to produce the hysteresis loops. At each field step, we computed equilibrium magnetic states by directly minimizing energy using the steepest descent method [35, 36] as implemented in MUMAX3. To simulate the (Fe-Co)-rich magnetic phase, we have assumed a saturation magnetization of $\mu_0 M_s = 2.1$ T and exchange stiffness of $A = 11$ pJ/m. To explore the coercivity's sensitivity to these inputs, we also varied M_s and A and found that H_c only changes a small amount if the ratio A/M_s remains constant. For example, doubling both M_s and A (for an ellipsoid with $D = 32$ nm and $c/a = 8$) yields a coercivity difference of less than 10%. Finite-temperature dynamic effects have not been considered explicitly, because they are known to yield well-understood logarithmically small magnetic-viscosity corrections [3, 25].

Figure 2 visualizes the initial stage of magnetization reversal, which is of the curling type, and shows the corresponding hysteresis loops. In the cuboids, the curling starts at the ends of the rod, in the middle of the short edges, propagates along the middle of the long faces, and eventually advances to the long edges and center of the rod. The curling mode in the ellipsoids is essentially delocalized throughout the rod, in agreement with exact analytic calculations [27]. Note the nonrectangular (curved) shape of the cuboid hysteresis loops.

It is straightforward to extract the coercivities from the calculated hysteresis loops. Figure 3 shows the coercivities of isolated rods of aspect ratio 8 as a function of width D for the square prism or diameter $D = 2R$ for the ellipsoid. The overall behavior, namely, that our coercivity results approach the Stoner-Wohlfarth value for very thin rods and nearly vanish for thick rods, is consistent with Eqs. (1) and (2). Furthermore, the square prism rods have smaller coercivity than the ellipsoids, in accordance with Eq. (1) since the demagnetizing field is inhomogeneous in square prisms.

Figure 4 analyzes the dependence of the coercivity on the aspect ratio of the rods. For ellipsoids, H_c slowly ap-

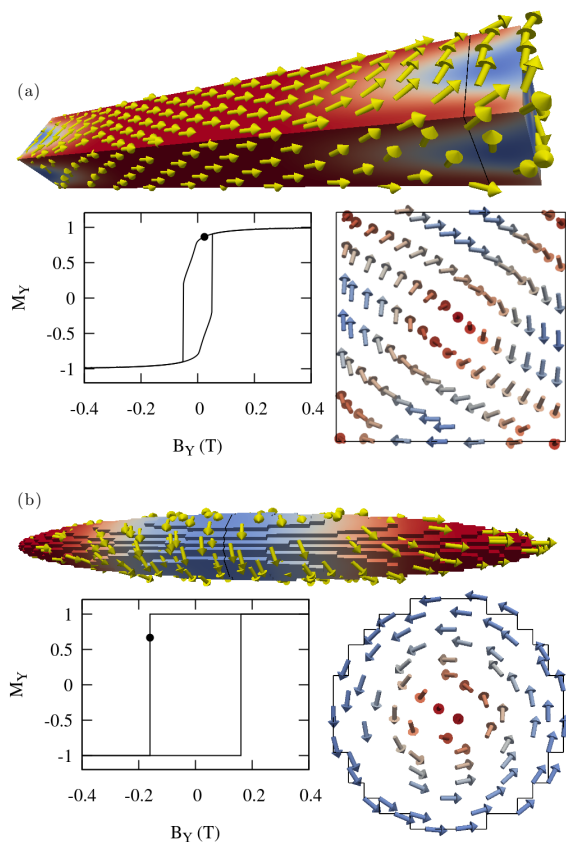


FIG. 2. Spin structures at the initial stage of curling for isolated Fe-Co (a) square prism and (b) ellipsoid surfaces and cross-sections. The corresponding fields and magnetizations are shown on the hysteresis loops. The surface coloring visualizes the magnetization along the field direction.

proaches a plateau value, because N_{\parallel} continues to change as the rods get longer. In contrast, H_c in both square prisms and cylinders barely changes above $c/a = 4$. The behavior of cylinders capped by ellipsoidal tips is intermediate between cylinders and ellipsoids, and the details depend on the aspect ratio of the tip, where hemispherical tips have little impact on the coercivity, but elongated tips improve it. This indicates that the geometry of the tip ends is more important than the aspect ratio and that ellipsoidal tips are (far) better than flat tips.

The green rectangle in Fig. 3 shows the range of rod diameters and coercivities typically encountered in laboratory-scale and industrial practice [6, 7]. Compared to the Stoner-Wohlfarth predictions (dashed line), the single-rod approximation of Figs. 1–3 reproduces the correct order of magnitude for coercivity. However, the quantitative agreement is, by no means, perfect. More importantly, interactions between rods are likely to modify the coercivity in a qualitative way. On a mean-field level, the magnetostatic interaction corrections are approximated by Eq. (1), but specific alnico interaction mechanisms have not yet been considered in the literature. Two classes of interactions need to be addressed:

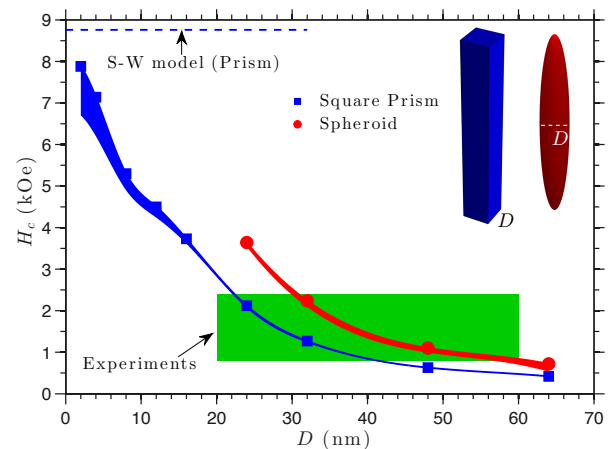


FIG. 3. Coercivity of isolated magnetic rods of aspect ratio 8 as a function of rod diameter. The Stoner-Wohlfarth limit for cuboidal rod is denoted by the dashed (blue) line. The thickness of the blue and red solid lines indicates the coercivity variation when the angle between the external field and rods varies from 1° to 5° . Typically observed alnico Fe-Co rod sizes and coercivities are denoted by the shaded (green) region.

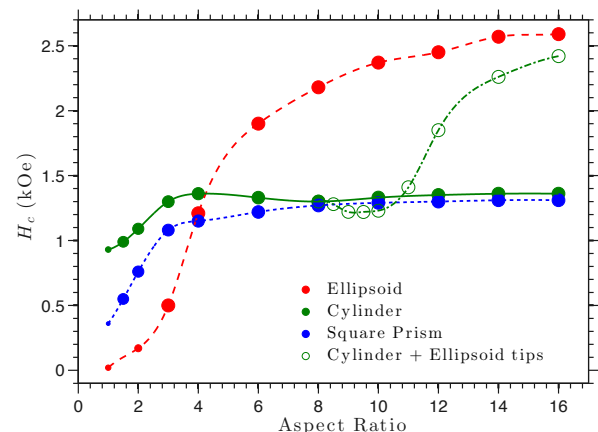


FIG. 4. Coercivity versus aspect ratio for different rod geometries. $D = 32$ nm in all cases. The ellipsoid-capped cylinders are constructed by capping a 256-nm-long cylinder with hemiellipsoids of various aspect ratio.

geometry-determined magnetostatic interactions and exchange interactions between bridging or branched rods.

To explore magnetostatic interaction effects, we have compared two arrangements of ellipsoidal rods, namely simple tetragonal (ST) rods and body-centered tetragonal (BCT) rods (Fig. 5). The ST array is constructed by repeating rods along the x , y , and z directions. The BCT geometry is a staggered array, where nearest-neighbor particles are shifted along the \parallel direction so that the center of the rods is between the tips of its eight neighboring rods. Periodic boundary conditions (PBCs) implemented using a so-called macrogeometry approach [37] were applied to simulate the assembly. Figure 5 compares the two arrangements for a constant packing fraction of

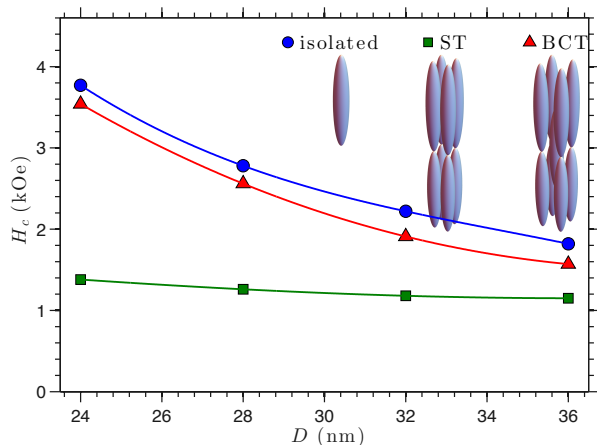


FIG. 5. Coercivity versus rod size for isolated ellipsoids and their assemblies (calculated using PBCs) with simple-tetragonal (ST) and body-centered tetragonal (BCT) patterns.

$p \approx 0.5$, an aspect ratio of 8, and a vertical end-to-end spacing of 1–2 nm. We see that the coercivity of the BCT array is about twice as high as the coercivity of the ST array. The reason for the difference is that tips with \uparrow magnetization act as poles and create a strong \downarrow field in the lateral neighborhood, adding to the reverse external magnetic field. The ST array has four laterally coordinated nearest neighbors, whereas in the BCT array, the nearest lateral neighbors are more distant. Furthermore, top and bottom tips form magnetic poles of opposite sign, which further reduces the lateral interaction effect for BCT array. For the coercivity of square prisms calculated using PBCs, the difference between ST and BCT arrays is smaller.

We have also calculated the coercivity of an *isolated* cluster of 64 ellipsoidal rods in a BCT arrangement, and the coercivities are very similar to those obtained by using PBCs. The $1 - p$ dependence of H_c on packing fraction, estimated using mean field as in Eq. (1), underestimates H_c in this case.

Strong exchange interactions are established through bridges and branching between rods. We have considered two parallel cuboid nanorods that are connected through different types of branching, namely, H-shaped, U-shaped, and O-shaped geometries. Figure 6 shows the coercivities as a function of the surface-to-surface distance d between rods. H-shape branching, where the rods are connected in the middle, is much less detrimental to coercivity than U- or O-shaped branching, where the rods are connected at the ends. This is because the magnetization reversal starts at the ends of the rods and is made easier by U- and O-branches in the vicinity. In the H-shape geometry, the reversal also starts at the rod ends, but the tips are still fairly isolated and the branches in the middle have a minor effect.

Interestingly, some of the above features are also encountered in fine-particle and nanowire magnetism

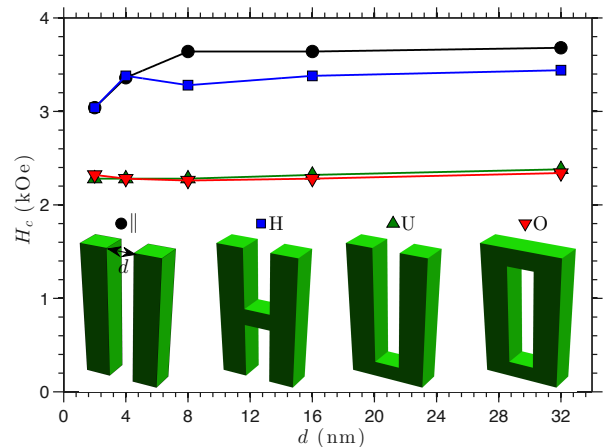


FIG. 6. Coercivity of free and connected rods as a function of the spacing d between rods. The individual rods have a width of 16 nm and an aspect ratio value of 8.

[22, 24, 38–42]. For example, fine particles also exhibit a transition from coherent rotation to curling, and wire-end features affect the coercivity [24, 25, 43]. Fine particles and embedded wires often have diameters small enough to approach Stoner-Wohlfarth H_c values but are nevertheless difficult to use as permanent magnets. The reason is that with their relatively small packing fraction p the energy product of a permanent magnet, which describes its performance [3], is quadratic in the magnetization and, therefore, quadratic in p . In contrast, the nanostructure of alnico results from spinodal decomposition via specific heat treatments and alnico packing fractions approach the “ideal value” of $p = 2/3$, depending on alloy composition. This yields relatively high magnetization levels but also strengthens the interactions between rods that can reduce coercivity.

In conclusion, we have used micromagnetic simulations to analyze the coercivity of alnico permanent magnets. We find strong deviations from the Stoner-Wohlfarth model caused by curling modes that are modified by the real structure of alnico alloys. Both the absolute coercivities and the coercivity trends are in good agreement with available experimental data. The shape, size, spacing, volume fraction, arrangements, and branching types of the magnetic Fe-Co rods in the nonmagnetic Ni-Al matrix all affect the coercivity, but aside from the packing fraction, the most important features are the shape of the rod ends or tips and interactions between them. These are all factors which are controlled by the chemistry and thermal-magnetic annealing of these alloys [7, 14, 44]. We predict that sharp ellipsoidal tips and a staggered arrangement of the rods should promote substantial coercivity improvements, but this morphology may also be the most difficult one to realize experimentally. Further research is necessary to see, for example, whether field annealing can be used to realize a staggered configuration and if optimized draw annealing can lead to rod tip “sharpening”.

Acknowledgment The authors are thankful to D. J. Sellmyer, W.-Y. Zhang, H.-W. Kwon, and K.-M. Ho for discussing several aspects of the present paper. This work was supported by the U.S. Department of Energy (DOE)

EERE-VT-EDT program under the DREaM project at the Ames Laboratory, which is operated for the U.S. DOE by Iowa State University under Contract No. DE-AC02-07CH11358.

-
- [1] J. F. Herbst, *Rev. Mod. Phys.* **63**, 819 (1991).
- [2] K. Kumar, *Journal of Applied Physics* **63**, R13 (1988).
- [3] R. Skomski and J. Coey, *Permanent magnetism* (Bristol: Institute of Physics Pub., 1999).
- [4] T. Mishima, *Ohm* **19**, 353 (1932).
- [5] R. M. Bozorth, *Ferromagnetism* (D. Van Nostrand Co., Princeton, New Jersey, 1951).
- [6] R. McCurrie, in *Handbook of Ferromagnetic Materials*, Vol. 3, edited by E. Wohlfarth (Elsevier, 1982) pp. 107–188.
- [7] L. Zhou, M. Miller, P. Lu, L. Ke, R. Skomski, H. Dillon, Q. Xing, A. Palasyuk, M. McCartney, D. Smith, S. Constantinides, R. McCallum, I. Anderson, V. Antropov, and M. Kramer, *Acta Materialia* **74**, 224 (2014).
- [8] N. Jones, *Nature* **472**, 22 (2011).
- [9] O. Gutfleisch, M. A. Willard, E. Brück, C. H. Chen, S. G. Sankar, and J. P. Liu, *Advanced Materials* **23**, 821 (2011).
- [10] J. Coey, *Scripta Materialia* **67**, 524 (2012).
- [11] S. Chu and A. Majumdar, *Nature* **488**, 294 (2012).
- [12] R. McCallum, L. Lewis, R. Skomski, M. Kramer, and I. Anderson, *Annual Review of Materials Research* **44**, 451 (2014).
- [13] R. Skomski, P. Manchanda, P. Kumar, B. Balamurugan, A. Kashyap, and D. J. Sellmyer, *IEEE Transactions on Magnetics* **49**, 3215 (2013), (invited).
- [14] L. Zhou, M. K. Miller, H. Dillon, A. Palasyuk, S. Constantinides, R. W. McCallum, I. E. Anderson, and M. J. Kramer, *Metallurgical and Materials Transactions E* **41**, 27 (2014).
- [15] Y. Sun, J. Zhao, Z. Liu, W. Xia, S. Zhu, D. Lee, and A. Yan, *Journal of Magnetism and Magnetic Materials* **379**, 58 (2015).
- [16] M. Zou, F. Johnson, W. Zhang, Q. Zhao, S. F. Rutkowski, L. Zhou, and M. J. Kramer, *Journal of Magnetism and Magnetic Materials* **420**, 152 (2016).
- [17] K. Löwe, M. Dürrschnabel, L. Molina-Luna, R. Madugundo, B. Frincu, H.-J. Kleebe, O. Gutfleisch, and G. C. Hadjipanayis, *Journal of Magnetism and Magnetic Materials* **407**, 230 (2016).
- [18] M. Fan, Y. Liu, R. Jha, G. S. Dulikravich, J. Schwartz, and C. C. Koch, *IEEE Transactions on Magnetics* **52**, 1 (2016).
- [19] L. Zhou, W. Tang, L. Ke, W. Guo, J. D. Poplawsky, I. E. Anderson, and M. J. Kramer, *Acta Materialia* **133**, 73 (2017).
- [20] J. Fidler and T. Schrefl, *Journal of Physics D: Applied Physics* **33**, R135 (2000).
- [21] F. E. Luborsky, L. I. Mendelsohn, and T. O. Paine, *Journal of Applied Physics* **28**, 344 (1957).
- [22] S. Chikazumi, *Physics of magnetism* (Wiley, New York, 1964).
- [23] W. F. Brown Jr, *Reviews of Modern Physics* **17**, 15 (1945).
- [24] H. Zeng, R. Skomski, L. Menon, Y. Liu, S. Bandyopadhyay, and D. J. Sellmyer, *Phys. Rev. B* **65**, 134426 (2002).
- [25] R. Skomski, *Journal of Physics: Condensed Matter* **15**, R841 (2003).
- [26] R. Skomski, *Simple Models of Magnetism*, Oxford Graduate Texts (OUP Oxford, 2008).
- [27] A. Aharoni, *Introduction to the Theory of Ferromagnetism*, International Series of Monographs on Physics, Vol. 93 (Oxford University Press, Oxford, 1996).
- [28] M. Donahue and R. McMichael, *Physica B: Condensed Matter* **233**, 272 (1997).
- [29] Y. Iwama, M. Takeuchi, and M. Iwata, *Transactions of the Japan Institute of Metals* **17**, 481 (1976).
- [30] R. Skomski, L. Ke, M. J. Kramer, I. E. Anderson, C. Z. Wang, W. Y. Zhang, J. E. Shield, and D. J. Sellmyer, *AIP Advances* **7**, 056222 (2017).
- [31] J. Fischbacher, S. Bance, M. Gusenbauer, A. Kovacs, H. Oezelt, F. Reichel, and T. Schrefl, in *Proc. REPM 2014* (Annapolis, Maryland, 2014) pp. 241–243.
- [32] R. Skomski, Y. Liu, J. Shield, G. Hadjipanayis, and D. J. Sellmyer, *Journal of Applied Physics* **107**, 09A739 (2010).
- [33] R. Skomski, G. Hadjipanayis, and D. J. Sellmyer, *IEEE transactions on magnetics* **43**, 2956 (2007).
- [34] R. Skomski, E. Schubert, A. Enders, and D. J. Sellmyer, *Journal of Applied Physics* **115**, 17D137 (2014).
- [35] A. Vansteenkiste, J. Leliaert, M. Dvornik, M. Helsen, F. Garcia-Sanchez, and B. Van Waeyenberge, *AIP Advances* **4**, 107133 (2014), MUMAX3 code can be found at <http://mumax.github.io>.
- [36] L. Exl, S. Bance, F. Reichel, T. Schrefl, H. Peter Stimming, and N. J. Mauser, *Journal of Applied Physics* **115**, 17D118 (2014).
- [37] H. Fangohr, G. Bordignon, M. Franchin, A. Knittel, P. A. J. de Groot, and T. Fischbacher, *Journal of Applied Physics* **105**, 07D529 (2009).
- [38] N. Poudyal and J. P. Liu, *Journal of Physics D: Applied Physics* **46**, 043001 (2013).
- [39] K. Gandha, K. Elkins, N. Poudyal, X. Liu, and J. P. Liu, *Scientific Reports* **4**, 5345 (2014).
- [40] P. Toson, A. Asali, W. Wallisch, G. Zickler, and J. Fidler, *IEEE Transactions on Magnetics* **51**, 1 (2015).
- [41] S. L. Vinas, R. Salikhov, C. Bran, E. M. Palmero, M. Vazquez, B. Arvan, X. Yao, P. Toson, J. Fidler, M. Spasova, U. Wiedwald, and M. Farle, *Nanotechnology* **26**, 415704 (2015).
- [42] D. Niarchos, G. Giannopoulos, M. Gjoka, C. Sarafidis, V. Psycharis, J. Rusz, A. Edström, O. Eriksson, P. Toson, J. Fidler, E. Anagnostopoulou, U. Sanyal, F. Ott, L.-M. Lacroix, G. Viau, C. Bran, M. Vazquez, L. Reichel, L. Schultz, and S. Fähler, *JOM* **67**, 1318 (2015).
- [43] F. Ott, T. Maurer, G. Chaboussant, Y. Soumare, J.-Y. Piquemal, and G. Viau, *Journal of Applied Physics* **105**, 013915 (2009).
- [44] J. W. Cahn, *Acta Metallurgica* **9**, 795 (1961).